

Experimental-numerical evaluation of a new butterfly specimen for fracture characterisation of AHSS in a wide range of stress states

This content has been downloaded from IOPscience. Please scroll down to see the full text.

2016 IOP Conf. Ser.: Mater. Sci. Eng. 159 012015

(<http://iopscience.iop.org/1757-899X/159/1/012015>)

View [the table of contents for this issue](#), or go to the [journal homepage](#) for more

Download details:

IP Address: 194.95.158.108

This content was downloaded on 05/04/2017 at 11:21

Please note that [terms and conditions apply](#).

You may also be interested in:

[Decomposition method based on a modified Arcan fixture and its application in an in situ combined load tester](#)

Zhichao Ma, Hongwei Zhao, Hongbing Cheng et al.

[A hybrid experimental-numerical technique for determining 3D velocity fields from planar 2D PIV data](#)

A Eden, M Sigurdson, I Mezi et al.

[Experimental and computational investigation of the effect of phase transformation on fracture parameters of an SMA](#)

Behrouz Haghgouyan, Nima Shafaghi, C Can Aydner et al.

[Finite-element modelling of non-destructive material evaluation: abibliography \(1976-1997\)](#)

J Mackerle

Experimental-numerical evaluation of a new butterfly specimen for fracture characterisation of AHSS in a wide range of stress states

I Peshekhodov, S Jiang, M Vucetic, A Bouguecha and B-A Berhens

Institute of Forming Technology and Machines (IFUM), Leibniz Universität Hannover
An der Universität 2, 30823 Garbsen, Germany

E-mail: peshekhodov@ifum.uni-hannover.de

Abstract. Results of an experimental-numerical evaluation of a new butterfly specimen for fracture characterisation of AHSS sheets in a wide range of stress states are presented. The test on the new butterfly specimen is performed in a uniaxial tensile machine and provides sufficient data for calibration of common fracture models. In the first part, results of a numerical specimen evaluation are presented, which was performed with a material model of a dual-phase steel DP600 taken from literature with plastic flow and fracture descriptions. In the second part, results of an experimental-numerical specimen evaluation are shown, which was conducted on another dual-phase steel DP600, which was available with a description of plastic flow only and whose fracture behaviour was characterised in the frame of this work. The overall performance of the new butterfly specimen at different load cases with regard to characterisation of the fracture behaviour of AHSS was investigated. The dependency of the fracture strain on the stress triaxiality and Lode angle as well as space resolution is quantified. A parametrised CrachFEM ductile shear fracture model and modified Mohr-Coloumb ductile shear fracture model are presented as a result of this quantification. The test procedure and results analysis are believed to contribute to current discussions on requirements to AHSS fracture characterisation.

1. Introduction

Driven by high energy costs and stringent legal regulations on CO₂ emissions during production and use of new vehicles, light-weight materials such as advanced high-strength steels with the ultimate tensile strength above 550 MPa (AHSS), aluminium and magnesium alloys as well as (fibre-reinforced) plastics are becoming extensively used in the automotive industry. According to a recent study of McKinsey & Company, the share of these materials in the global car production accounted for 29 % in 2010 and is expected to grow up to 67 % by 2030 [1]. Thereof, AHSS are expected to show the largest growth in absolute numbers from 15 % to 38 %. As opposed to the AHSS, the use of steels with the ultimate tensile strength below 550 MPa is anticipated to decline drastically from 52 % in 2010 to 13 % in 2030 [1]. As a result of these two expected changes, a noteworthy reduction of the overall steel share in the material mix of this mass-production industry from 67 % to 51 % over the span of twenty years is predicted [1]. To possibly make this decline less pronounced, the steel manufactures are forced to work continuously on improvement of existing AHSS on one hand and on new solutions for a better exploitation of their advantageous properties in car manufacturing on the other.



A better exploitation of AHSS in car manufacturing can be facilitated by FEA-based design of their forming and crash. This requires a mathematical formulation of the yield condition, hardening behaviour and formability. For decades, the forming limit curve (FLC) has been used to describe sheet metal formability [2]. Despite these limitations, such as its validity for linear strain paths and plane stress states ranging from uniaxial tension to equibiaxial tension, the accuracy of failure prediction based on the FLC is acceptable for conventional deep-drawing steels, but not for all AHSS [3]. Especially for shear-dominated stresses or bending loads alternative formability descriptions are required for AHSS [4]. For steel manufacturers it is therefore crucial to provide such alternative formability descriptions along with their AHSS.

As an alternative to the FLC to predict sheet metal failure, fracture models can be considered. In these models, fracture initiation is predicted based on a relation between the equivalent plastic strain $\bar{\varepsilon}_{pl}$ and the equivalent plastic strain at fracture $\bar{\varepsilon}_{pl}^f$ (or fracture strain for simplicity). The fracture strain is a material characteristic, which depends on the stress state at which plastic deformation occurs. Many formulations exist for the dependence of the fracture strain on the stress state [5, 6, 7]. To quantify the stress state, the stress triaxiality η and normalised Lode angle $\bar{\theta}$ are becoming often used in the analysis of sheet metal forming and crash [8, 9].

A number of different specimens and tests can be currently used to calibrate fracture models. Still, fracture strains of AHSS are scarce in literature and if found, they often differ much from one author to another for similar or even the same steel grades [10, 11, 12]. The large discrepancies in fracture strains of different authors can be explained with the fact that there currently exist neither consistent requirements nor recommendations to the geometry of the material specimens, test procedures and results analysis for their determination [13, 14].

The paper presents an experimental-numerical evaluation of a new butterfly specimen for fracture characterisation of AHSS. The shape of the specimen is similar to that of the specimens proposed by Mohr and Henn [15] and Bai [16] but has geometry modifications, which make the position of the crack initiation more predefined, reduce the test sensitivity on the specimen holder displacement and act against undesired material thinning. The test is performed in a uniaxial tensile testing machine and provides sufficient data for calibration of common fracture models. In the first part of the paper, results of a numerical specimen evaluation are presented, which was performed with a material model of a dual-phase steel DP600 taken from literature [17] with both plastic flow and fracture behaviour descriptions. With the help of this numerical evaluation, spatial distribution of the equivalent plastic strain and damage variable in the specimen as well as time variation of the stress state at the location of fracture initiation were investigated. In the second part of the paper, results of an experimental-numerical test evaluation are shown, which was conducted on another dual-phase steel DP600 of 1.4 mm thickness, which was available with a description of plastic flow only and whose fracture behaviour of AHSS was characterised in the frame of this work. With the help of this experimental-numerical evaluation, the performance of the new butterfly specimen with regard to characterisation of the fracture behaviour was investigated. Finally, modelling of the DP600 fracture behaviour with the help of the CrachFEM ductile shear fracture model and modified Mohr-Coloumb fracture model is discussed.

2. Numerical evaluation

2.1. Material

The evaluation was performed on a dual-phase steel DP600 of 1.4 mm. To model the yield behaviour, the Hill'48 yield condition and an isotropic hardening formulation were taken from literature [17] and are graphically presented in figure 1. To describe the fracture behaviour, the CrachFEM ductile shear fracture model [6] was used:

$$\bar{\varepsilon}_{pl}^f = \frac{\bar{\varepsilon}_{pl}^{f+} \cdot \sinh(f \cdot (\gamma^- - \gamma)) + \bar{\varepsilon}_{pl}^{f-} \cdot \sinh(f \cdot (\gamma - \gamma^+))}{\sinh(f \cdot (\gamma^- - \gamma^+))}, \quad (1)$$

where $\gamma = (1 - k_{sf} \cdot \eta) / (\tau_{\max} / \bar{\sigma})$ is the shear stress parameter with k_{sf} being the stress triaxiality weight factor, τ_{\max} being the maximum shear stress and $\bar{\sigma}$ being the von Mises equivalent stress, γ^- and γ^+ are the shear stress parameters at equibiaxial compression and equibiaxial tension respectively, $\bar{\varepsilon}_{pl}^{f-}$ and $\bar{\varepsilon}_{pl}^{f+}$ are the fracture strains at equibiaxial compression and equibiaxial tension and f is a model coefficient. The model input parameters are summarized in table 1 [17]. A graphical representation of the model is given in figure 2 [17].

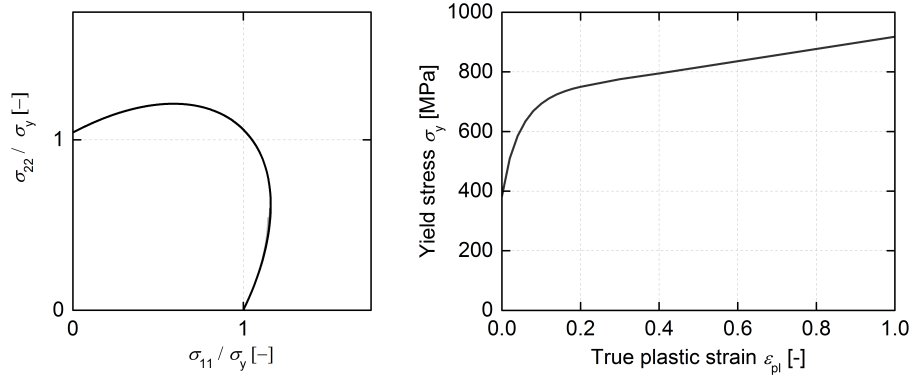


Figure 1. Yield locus (left) and yield curve (right) of DP600 [17]

Table 1. Coefficients of the CrachFEM shear fracture model of DP600 [17]

k_{sf} [-]	f [-]	γ^+ [-]	γ^- [-]	$\bar{\varepsilon}_{pl}^{f+}$ [-]	$\bar{\varepsilon}_{pl}^{f-}$ [-]
0.120	2.500	1.840	2.160	0.900	1.900

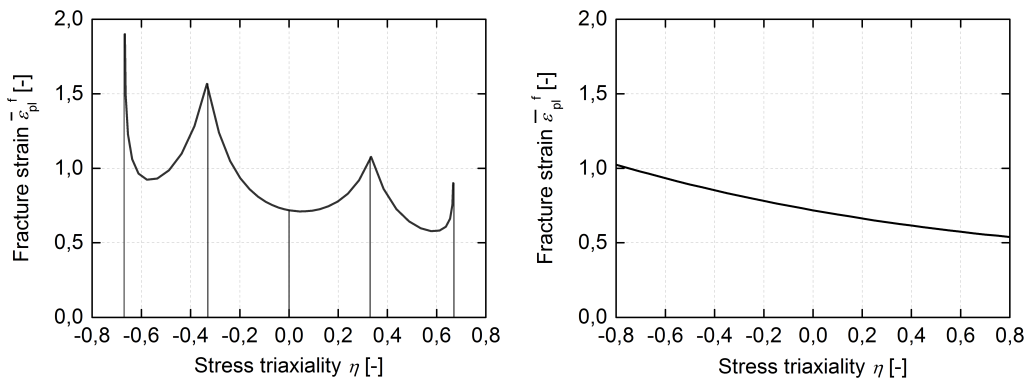


Figure 2. Fracture curve of DP600 for plane stress states (left), plane strain states (right) [17]

At each increment of the FEA, the incremental equivalent plastic strain $\bar{\varepsilon}_{pl,i}$ in a particular finite element is divided by the fracture strain $\bar{\varepsilon}_{pl}^f$, which is characteristic for the stress state acting in this element during this increment. The division product is then to be accumulated over the increments to obtain the variable D defined by:

$$D = \sum_i \frac{\bar{\varepsilon}_{pl,i}}{\bar{\varepsilon}_{pl}^f}, \quad (2)$$

which is referred to as damage variable. At an increment of $D \geq 1$ fracture initiation is assumed.

2.2. Finite element model

The new specimen, the geometry of which is similar to that of the specimens proposed by Mohr and Henn [15] and Bai [16], is shown in figure 3 and can be divided into the following areas:

- two load introduction areas over which the external load is introduced from the specimen holder into the specimen via friction forces (1.1 and 1.2),
- one load transfer area with a material cutout on the left and on the right side of the specimen, which follows a smooth concave-convex curve (2),
- one analysis area with reduced material thickness by 25 % of the initial sheet thickness from each of the two sheet sides, which is entirely enclosed within the load transfer area along a smooth concave-convex loop (3).

The interaction of the load transfer area and analysis area lead to localisation of plastic strain in the middle of the analysis area independent of the direction of the load applied in the sheet plane. Thus, the first crack initiates in the material interior and not at the specimen edge. This ensures that the material formability at a desired stress state and not the specimen edge formability at a uniaxial stress state is determined. The specimen is extracted from the sheet with the help of wire erosion so that the longer side of the specimen is oriented parallel to the rolling direction of the sheets. The thickness reduction in the analysis area is carried out by means of machining, whereby the roughness of $R_a < 0.8$ and $R_z < 6.3$ or finer is ensured [18].

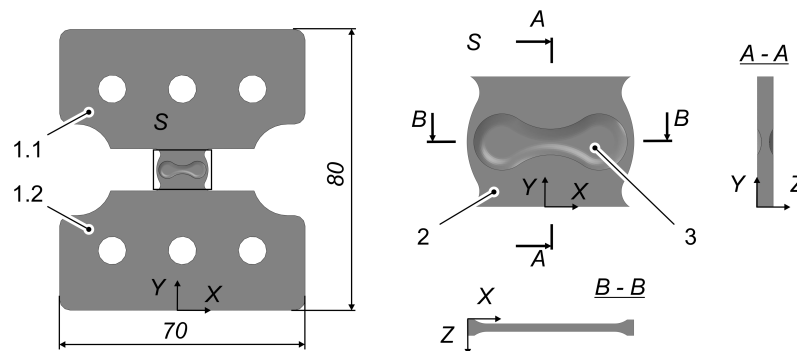


Figure 3. Geometry of the new butterfly specimen with two load introduction areas (1.1 and 1.2), one load transfer area (2) and one analysis area (3)

The stress and strain fields in the new specimen and specimen of Bai [16] due to a load arbitrary oriented in the specimen plane were investigated with a FE model shown in figure 4. Parts of the specimen holder and the fastening plates, which come into contact with the specimen were modelled as elastic bodies. The specimen was clamped between the specimen holder and the fastening plates with the help of pressure of $p_z = 204$ MPa applied to six circle areas on the fastening plates, which imitate the contact areas beneath the disks of the six screws. The magnitude of the pressure was chosen to correspond to a fastening moment on a M8 screw of 35 Nm. 3D volume elements were used to realistically represent the stress state in the material, especially beyond the onset of plastic strain localisation. In particular, sufficiently fine (0.1 mm) continuum eight-node linear reduced-integration elements with an hourglass control as provided in the element library of Abaqus/Standard under the notation C3D8R were used for specimen areas of large deformations. Furthermore, a thin layer of complaint shell elements was applied to one of the specimen surfaces for evaluation of strain paths. The specimen deformation was induced by applying a displacement u_{xy} on all the outer surface nodes of one of the specimen holders. The direction of the displacement u_{xy} was defined by the load application angle α . The following α were investigated: -3.0° , 12.5° , 28.0° , 43.5° , 59.0° , 74.5° and 90.0° , each of them stayed constant during the corresponding test.

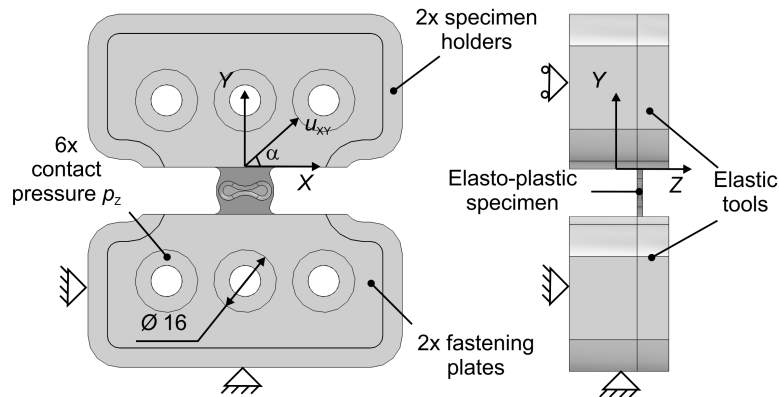


Figure 4. Components and boundary conditions of the finite element model of a tensile test on butterfly specimen according to Bai [16] and new butterfly specimen

2.3. Results and discussion

The objectives of the performed geometry optimisation of the new butterfly specimen as compared to the butterfly specimen according to Bai [16] were:

- contraction of the zone of high plastic deformation along the shorter side of the specimen,
- extension of the zone of high plastic deformation along the longer side of the specimen,
- suppression of material thinning in the zone of high plastic deformation.

To reach the objectives, the curvature radius of the waist of the analysis area both in the specimen plane and in the plane orthogonal to it was decreased. Furthermore, the analysis area of reduced material thickness was completely enclosed into the load transfer area of the initial material thickness. The latter leads to two outwardly convex bridges of the initial material thickness connecting the two opposite sides of the specimen, which support the stress state and act against material thinning. An exemplary result of the optimisation is shown in figure 5.

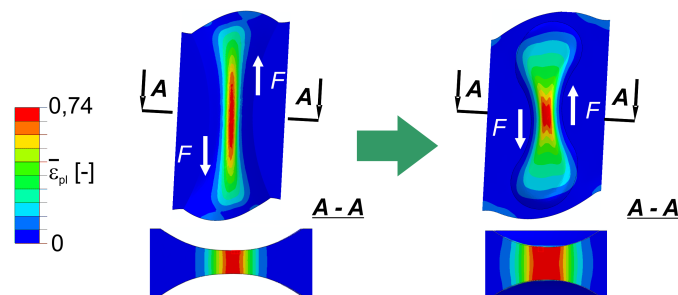


Figure 5. Equivalent plastic strain in the butterfly specimen according to Bai [16] (left) and new butterfly specimen (right) at the moment of fracture initiation for $\alpha = -3.0^\circ$

Figure 5 illustrates the contraction of the zone of high plastic deformation along the shorter side of the specimen and its extension along the longer side of the specimen. This increases the safety of fracture initiation at a desired stress state as demonstrated in figure 6. For the diagrams in figure 6, it was assumed that due to inhomogeneity of the real material formability fracture initiation may take place at any finite element in which the condition $D \in [0.98 \cdot D_{\max}; D_{\max}]$ with $D_{\max} \geq 1$ is satisfied. Under this assumption, figure 6 shows that the differences in the stress triaxialities among possible locations of fracture initiation is lower for the new butterfly specimen.

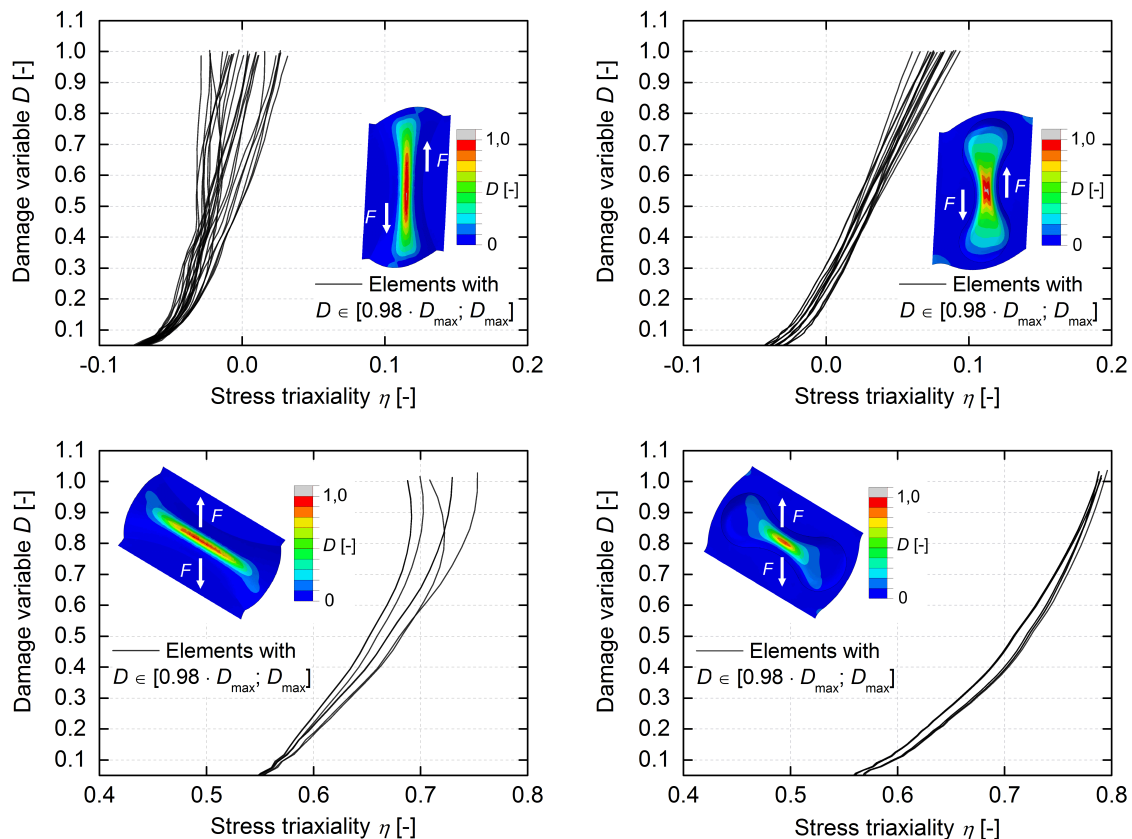


Figure 6. Stress triaxiality in the elements of potential fracture initiation for the butterfly specimen according to Bai [16] (left) and new butterfly specimen (right) for $\alpha = -3^\circ$ (top) and $\alpha = 59^\circ$ (bottom)

Figure 5 also illustrates the extension of the zone of high plastic deformation along the longer side of the specimen. This favourably decreases the sensitivity of the equivalent plastic strain at the location of fracture initiation to the relative displacement of the opposite specimen holder parts as presented in figure 7. This decreased sensitivity allows a more accurate fracture characterisation with the help of conventional uniaxial tensile testing machines.

Finally, the effect of the enclosure of the analysis area of reduced material thickness with the load transfer area of initial material thickness on the stress state is illustrated in figure 8. The stress state in the new butterfly specimen is slightly less sensitive to the variation of the load application angle. In other words, a more accurate definition of the desired stress state via definition of the load application angle is possible. For stress triaxialities $\eta > 0.33$ at the location of fracture initiation, the new butterfly specimen exhibits less local material thinning. This becomes manifest in lower variation of the stress triaxiality at the fracture initiation location.

The analysis of damage variable distribution in the analysis area of the new butterfly specimen obtained for the studied seven load application angles reveals that the fracture initiation is expected at the surface of the analysis area for $\alpha = -3.0^\circ$ and $\alpha = 12.5^\circ$ and is likely to occur at the surface of the analysis area for $\alpha = 28.0^\circ$ as shown in figure 9, top. For these load application angles, fracture initiation takes place due to plastic deformation at plane stress states and the fracture strain can be determined with the help of digital image correlation of sufficiently fine resolution (specimen surface). On the contrary, the maximum damage variable is reached in the middle of the specimen for $\alpha = 43.5^\circ$, $\alpha = 59.0^\circ$, $\alpha = 74.5^\circ$ and $\alpha = 90.0^\circ$

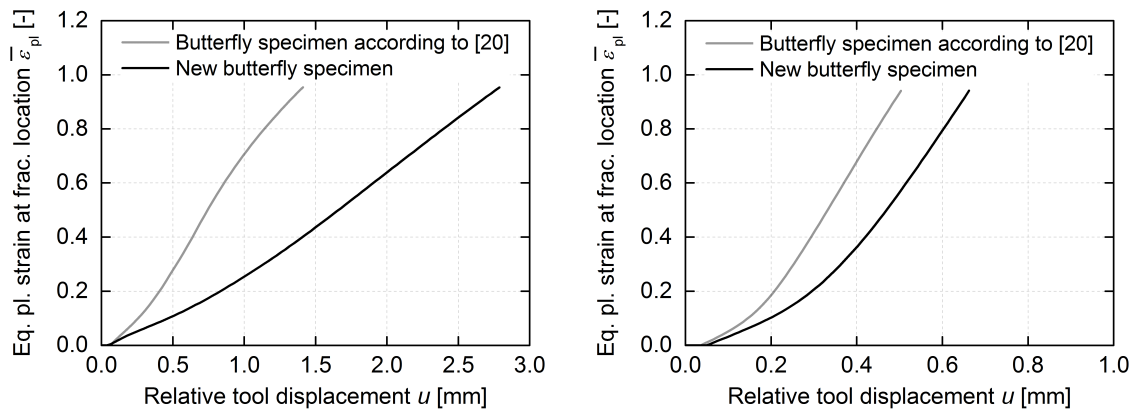


Figure 7. Equivalent plastic strain at the location of fracture initiation versus tool displacement for the butterfly specimen according to [16] and proposed butterfly specimen for the load application angle $\alpha = -3^\circ$ (left) and $\alpha = 59^\circ$ (right)

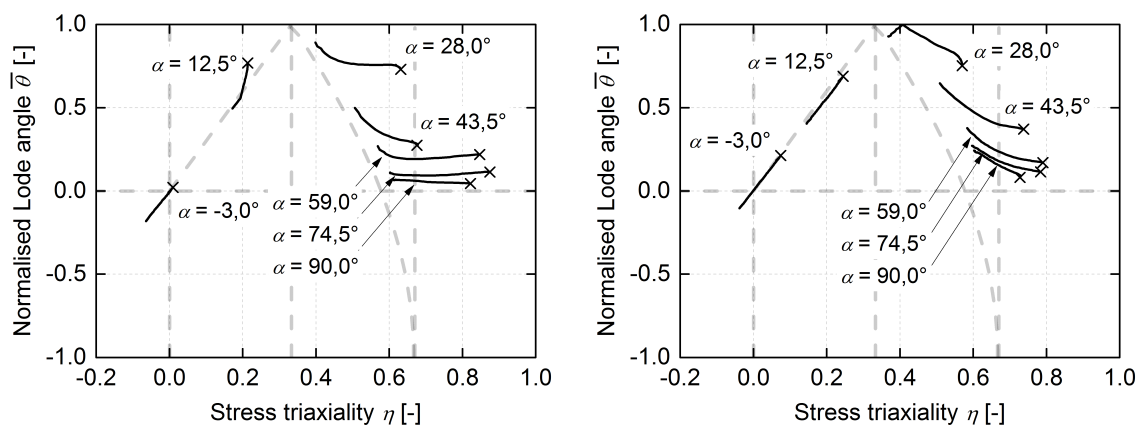


Figure 8. Development of the stress state at the location of fracture initiation for the butterfly specimen according to Bai [16] (left) and the new butterfly specimen (right) for α

as shown in figure 9 bottom. For these load application angles, fracture initiation takes place due to plastic deformation at three-dimensional stress states and other methods like FEA are required to determine the fracture strain (specimen middle). The transition between these two characteristic locations of fracture initiation in the tensile tests on the new butterfly specimen occurs at the stress triaxiality of $\eta \approx 0.33$.

As a last result, development of the stress states at the location of fracture initiation in the space of the stress triaxiality and equivalent plastic strain as well as development of the strain state at the most deformed material point at the surface in the space of the second major strain and first major strain are presented in figure 10. From figure 10 it can be seen that the change of the load application angle from $\alpha = -3.0^\circ$ to $\alpha = 43.5^\circ$ goes along with a change of the stress triaxiality, whereas the change of the load application angle from $\alpha = 43.5^\circ$ to $\alpha = 90.0^\circ$ lead only to minor changes of the stress triaxiality and is rather characterised by a change of the normalised Lode angle (compare figure 8, right and figure 10, left). The strain paths at the most deformed material point at the surface for different load application angles are presented in figure 10, right and cover the range of strain states from pure shear to plane strain.

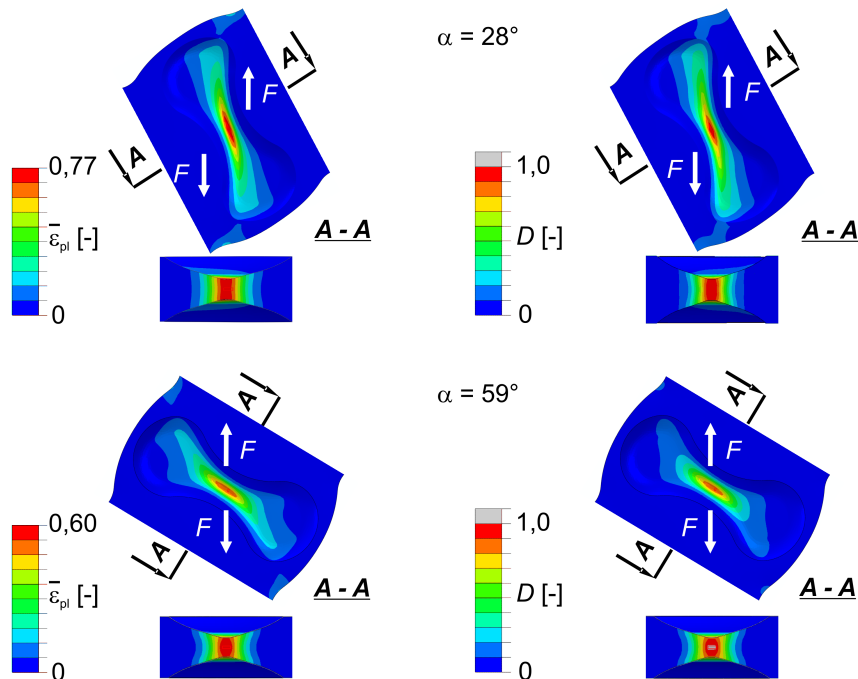


Figure 9. Equivalent plastic strain (left) and damage variable (right) in the proposed butterfly specimen at the moment of fracture initiation for $\alpha = 28.0^\circ$ (top) and $\alpha = 59.0^\circ$ (bottom)

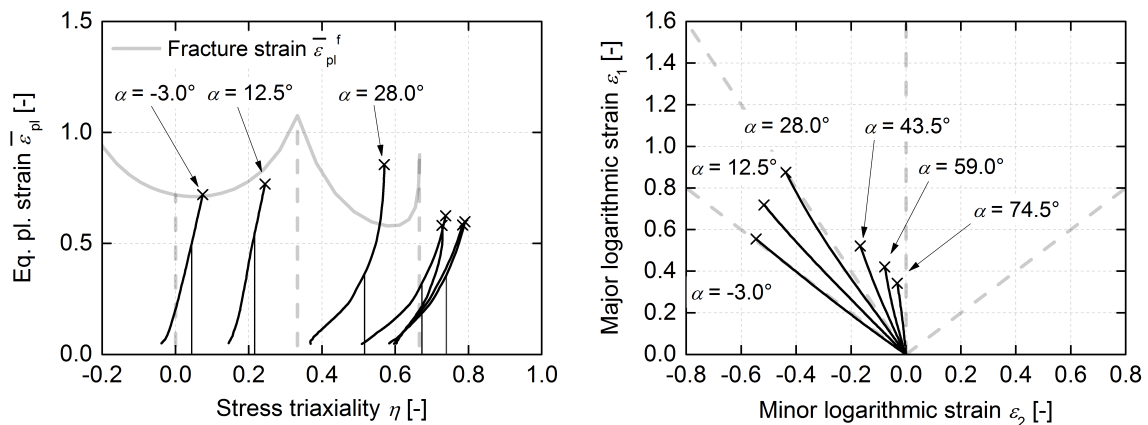


Figure 10. Stress state at the location of fracture initiation (left) and strain path at the location of the highest equivalent plastic strain on the specimen surface (right) of the new specimen

3. Experimental-numerical evaluation

3.1. Experimental set-up

The tests on the new butterfly specimen were realised in a uniaxial tensile testing machine with the help of a tool shown in figure 11, left. The tool consists of two fixtures which are firmly attached to the pistons of the machine and have a slot to accommodate two half-disk-shaped specimen holders. The specimen holders can be adjusted in this slot allowing a desired specimen orientation relative to the test load direction. Each fixture and the corresponding specimen holder have seven holes through which pins are inserted to lock the specimen holders

in a particular orientation and prevent them from rotating during the test. The tool allows the following load application angles of -3.0° , 12.5° , 28.0° , 43.5° , 59.0° , 74.5° and 90.0° , which remain constant during the test. The tests were carried out with the piston speed of 0.05 mm/s to ensure quasistatic deformation. During the tests, deformation of the analysis area of the specimen was continuously recorded with the help of the optical measurement system Aramis (GOM mbH) as shown in figure 11, right. Furthermore, the relative displacement of two reference points on the opposite specimen holders close to the analysis area of the specimen were optically recorded. The relative displacement of these two reference points at the moment of fracture initiation provided the boundary conditions for the FEA of the tests.

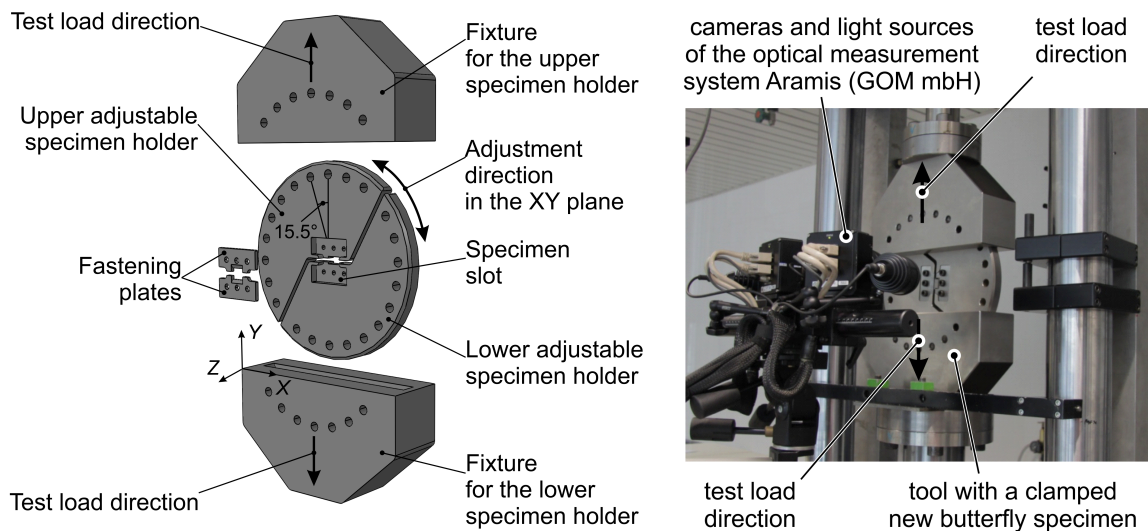


Figure 11. Tool (left) and set-up (right) for tensile tests on the new butterfly specimen

3.2. Material

A DP600, 1.4 mm, produced by Salzgitter Flachstahl GmbH was used. The elastic behaviour of the material was described with the elastic modulus of 210 GPa and the Poisson ratio of 0.3. The plastic behaviour was modelled with the Hill'48 yield condition with $F = 0.460$, $G = 0.534$, $H = 0.466$, $N = 1.366$, $L = 1.500$ and $M = 1.500$ [18] and a combined Swift-Hockett-Sherby model determined with the help of uniaxial tensile and hydraulic bulge tests [19] given by

$$\sigma = 0.479 \cdot \left(642 \cdot \left(0.00596 + \bar{\epsilon}_{pl} \right)^{0.660} \right) + 0.521 \cdot \left(1224 - (1224 - 757) \cdot e^{-15.5 \cdot \bar{\epsilon}_{pl}^{0.820}} \right) \quad (3)$$

3.3. Finite element model

The numerical analysis of the tests was performed to determine the development of stress state and equivalent plastic strain at the location of fracture initiation over time. The location of fracture initiation was assumed based on the results of the numerical evaluation of the test from the previous chapter, which was performed with both the plasticity model and fracture model for another DP600 from [17]. The same finite element model schematically shown in figure 4 was used. The relative tool displacement for each of the seven load application angles was set to be equal to the relative tool displacement obtained in the experiment for the corresponding load application angle at the moment of fracture initiation. Three element sizes were used to investigate the dependence of the fracture strain on the space resolution: 0.025 mm, 0.100 mm and 0.180 mm. It should be noted here that element with the edge length of 0.2 mm are the largest elements, which can be used to accurately model geometry of the new butterfly specimen.

3.4. Results and discussion

The finite element model used in the study was validated based on a comparison of the experimentally and numerically determined test forces, which are exemplary shown for the two extreme load application angles in figure 12, left. It can be concluded that the quality of the used material description and boundary conditions is acceptable. The high scatter of the test force at the load application angle $\alpha = 90.0^\circ$ is mainly explained with the scatter of the material thickness in the analysis area of the specimen and not with the scatter of the material properties. Figure 12, right shows representative strain paths determined with the help of digital image correlation (DIC) for the load application angles, which lead to fracture initiation at the specimen surface (plane stress states). The strain paths in figure 12 are deliberately shown for small and medium strains only as at higher strains the data determined with DIC went corrupt due to excessive shear deformation of the paint pattern applied to the surface.

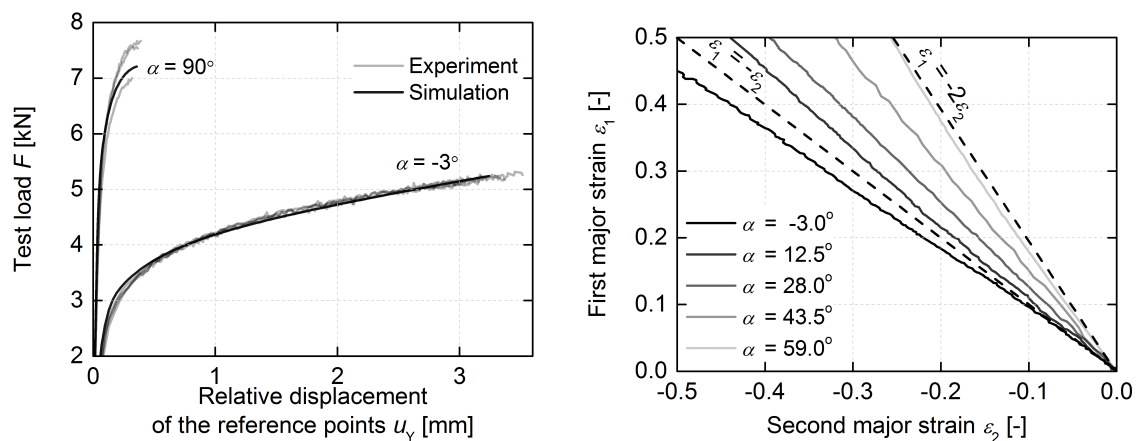


Figure 12. Exemplary experimentally and numerically determined test forces (left) and optically determined strain paths at the location of the highest deformation (right)

The development of the stress state at the location of fracture initiation is presented in figure 13. Based on the results of the numerical test evaluation given in the previous chapter, it is assumed that fracture initiation takes place at the surface of the analysis area due to plastic deformation at plane stress states for the load application angles α of -3.0° , 12.5° , 28.0° , 43.5° and 59.0° and in the middle of it due to plastic deformation at 3D stress states for the load application angles α of 74.5° and 90.0° . Due to the horizontal movement of the specimen holders, a stress state shift towards lower stress triaxialities is observed (figure 10, left and figure 13, right). In figure 13, right the characteristic stress states for each load application angle are denoted by the thin black lines. The characteristic stress state parameters were determined as a weight centre of the area below the corresponding curve as used by e. g. Wierzbicki et al. [7].

The equivalent plastic strain at the location of fracture initiation numerically determined for the tool displacement, at which fracture initiation took place in the experiment was defined to be the fracture strain. The so determined fracture strain was found to be dependent on the size of the finite elements or, in other words, on the space resolution. This dependency was found to be linear in the studied range of the virtual strain gauge lengths l_0 and is in its turn stress state dependent as shown in figure 14, left. The space resolution dependency of the equivalent plastic strain is intrinsic for ductile materials exhibiting strain localisation and is more pronounced for triaxial tensile stress states. In the present work, it is considered with the help of equation 4, which is constructed based on the obtained numerical results for three different finite element sizes (or virtual strain gauge lengths l_0) mentioned above. The dependency of the virtual strain

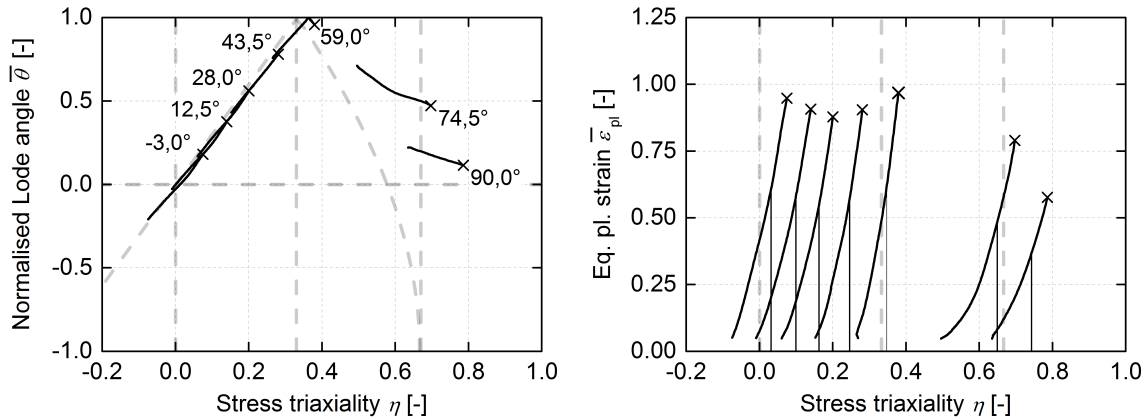


Figure 13. Stress state at the location of fracture initiation in the tensile tests on the new butterfly specimen with an indication of the characteristic stress state of DP600

gauge length factor b on the stress triaxiality is shown in figure 14, right.

$$\bar{\varepsilon}_{pl}^f(l_0) = \bar{\varepsilon}_{pl}^f(l_0 = 0) + b \cdot l_0, \quad (4)$$

where $\bar{\varepsilon}_{pl}^f(l_0)$ is the fracture strain for the strain gauge length l_0 and b is the strain gauge length factor from table 2. It should be noted that equation 4 is valid for $l_0 \in [0.02 \text{ mm}; 0.2 \text{ mm}]$. The results of the performed determination of the input data for parametrisation of fracture models for three different space resolutions are summarised in table 2. A comparison of the fracture data with the fracture data obtained by Basaran [20] for a DP600 of 1.0 mm and $l_0 = 0.075 \text{ mm}$ is presented in figure 15, right and reveals a good accordance.

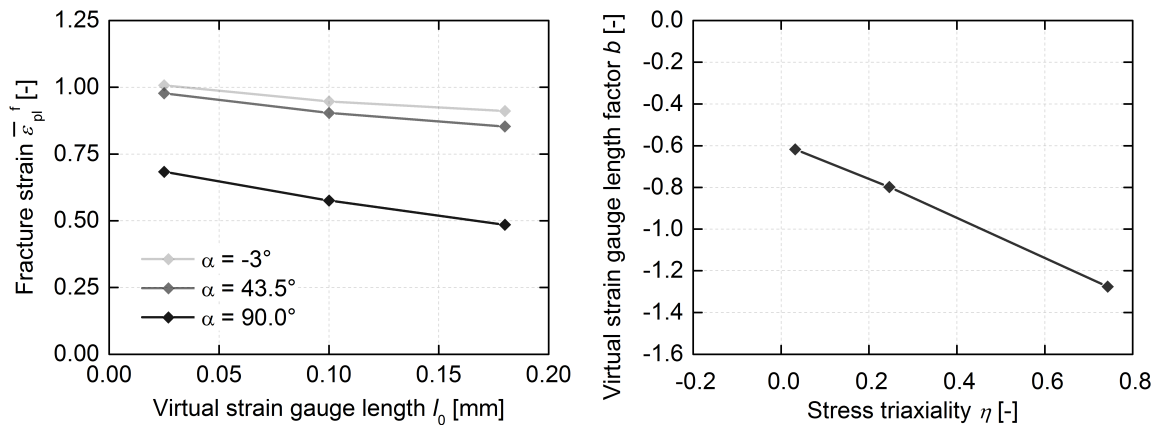
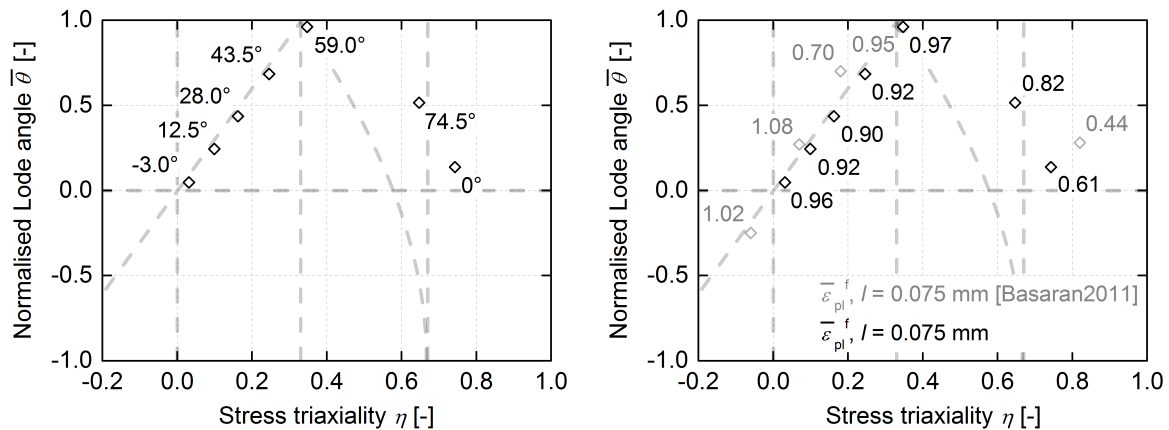


Figure 14. Fracture strain versus virtual strain gauge length for different α (left) and dependence of the virtual strain gauge length factor on the stress triaxiality (right) for DP600

The data from table 2 was subsequently approximated with the CrachFEM ductile shear fracture model given by equation 1. The model parameters are in table 3. A comparison of the graphical representation of the CrachFEM model from [17] and graphical representation of the CrachFEM model determined in this work is given in figure 16. From the comparison it can be seen that the mean positions of the two fracture surfaces with regard to the fracture strain

Table 2. Exp.-numerical results of the tensile tests on the new butterfly specimen of DP600

Load appl. angle α [°]	Stress triaxiality η [-]	Normalised Lode angle $\bar{\theta}$ [-]	Fracture strain $\bar{\varepsilon}_{pl}^f$ for the strain gauge length $l = 0.01$ mm [-]	Strain gauge length factor b acc. to equation 4 [-]
-3.0	0.032	0.047	0.947	0.610
12.5	0.100	0.243	0.907	0.673
28.0	0.162	0.436	0.878	0.731
43.5	0.246	0.683	0.904	0.809
59.0	0.348	0.960	0.941	0.990
74.5	0.649	0.514	0.790	1.183
90.0	0.743	0.144	0.576	1.272

**Figure 15.** Characteristic stress states at the location of fracture initiation (left) and comparison of the test results with those of Basaran [20] (right) for $l = 0.075$ mm and DP600

axis are similar. The difference between the two lies in the dependence of the fracture strain on the normalised Lode angle. This dependence was found to be less pronounced for the fracture surface determined in this work as compared to the fracture surface from [17]. The shape of the fracture surface of DP600 determined in this work correlates well with the results of Basaran [20]. It can be concluded that the dependence of the fracture strain of DP600 on $\bar{\theta}$ is not that pronounced as it is often assumed to be as e. g. in [17]. A reasons for the higher curvature of the fracture surface along the normalised Lode angle axis in [17] may be inaccurate determination of the fracture strain in the shear test. As shown by Behrens et al. [17], the use of an ASTM-similar shear specimen in the shear test can lead to underestimated values of the fracture strain and, hence, to a more curved fracture surface along the normalised Lode angle axis.

The dependence of the fracture strain on the virtual strain gauge length l_0 is illustrated in figure 17. From figure 17, it can be clearly seen that the dependence of the fracture strain on the virtual strain gauge length l_0 is more pronounced for higher stress triaxialities and can be neglected for compression-dominated stress states characterised by $\eta < -0.33$. This behaviour of the material in the FEA can be explained with plastic strain localisation prior to fracture, which is better resolved by finer finite elements leading to higher values of computed strains. Naturally, the degree of plastic strain localisation is defined by the stress state.

Table 3. Coefficients of the CrachFEM shear fracture model of DP600

l [mm]	k_{sf} [-]	f [-]	γ^+ [-]	γ^- [-]	$\bar{\varepsilon}_{pl}^{f+}$ [-]	$\bar{\varepsilon}_{pl}^{f-}$ [-]
0.020	0.259	0.1490	1.655	2.346	0.910	1.360
0.100	0.340	0.0213	1.546	2.454	0.802	1.360
0.200	0.436	0.0490	1.418	2.582	0.671	1.360

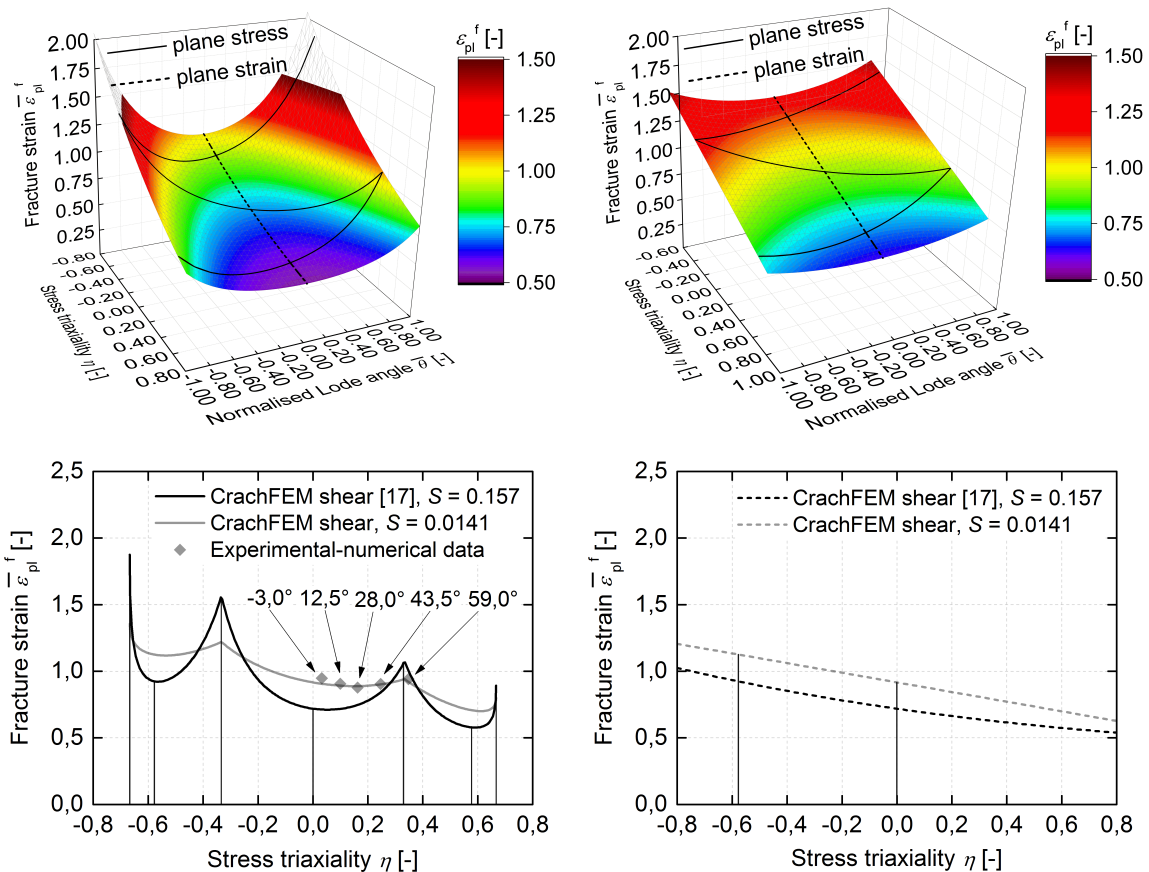


Figure 16. Fracture surface of DP600 according to the CrachFEM model from [17] (top left) and CrachFEM model from this work for the virtual gauge length of 0.1 mm (top right) and fracture curves for plane stress states (bottom left) and plane strain states (bottom right) with S being the sum of squared residuals

Finally, the fracture data from table 2 for the virtual strain gauge $l_0 = 0.2$ mm was approximated with the modified Mohr-Coulomb shear fracture model [21], which can also be used to predict fracture initiation in AHSS [22]. The determined model parameters are summarised in table 4. It should be noted here, however, that not the original MMC model [21], which corresponds to a combination of the Mohr-Coulomb fracture criterion with a Lode-angle-dependent plasticity model, is used. Instead, an inconsistent version of the MMC model, as discussed e.g. by Mohr and Marcadet [23], which is just a fitting function for the fracture data is made use of. A comparison of the fracture surfaces is presented in figure 18. The deviations of the model predictions from the seven data points used for their parametrisation can be seen from table 5. From figure 18 and table 5 it can be seen that both models approximate the

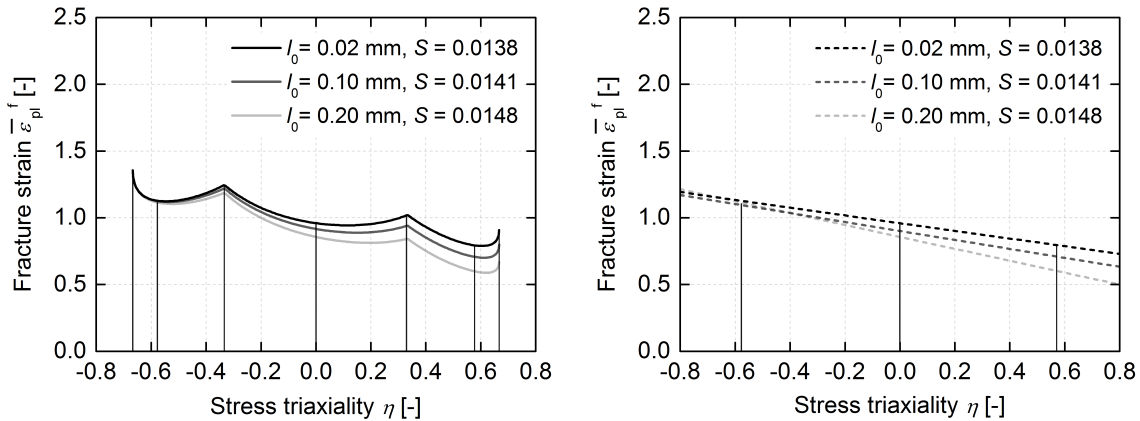


Figure 17. Fracture curves of DP600 according to the CrachFEM shear fracture model for different virtual strain gauges l_0 at plane stress states (left) and plane strain states (right)

fracture data similarly and accurately enough. In the present study, the focus is put on fracture characterisation at shear-dominated stress states of $\eta \in [0; 0.33]$. In this range both models perform equally well. The difference between the two becomes notable for $\eta < 0$. In the case of the symmetric shape of the fracture surface given by the CrachFEM model with regard to $\bar{\theta} = 0$, the increase of the fracture strain at plane stress states with a decreasing stress triaxiality in the range of $\eta \in [-0.33; 0]$ is defined by the overall slope of the fracture surface along the stress triaxiality axis. On the contrary, the asymmetry of the fracture surface given by the MMC model with regard to $\bar{\theta} = 0$ allows a steeper increase of the fracture strain at plane stress states with a decreasing stress triaxiality in the range of $\eta \in [-0.33; 0]$. Therefore, the MMC fracture model parameterised with the fracture data from table 2 may give slightly better predictions of fracture initiation due to plastic deformation at compression-superimposed shear stress states characterised by $\eta \in [-0.33; 0]$. Plastic deformation at such stress states may occur, for example, in the flange area of a sheet in a deep-drawing process.

Table 4. Coefficients of the MMC shear fracture model of DP600

l [mm]	A [-]	n [-]	C_1 [-]	C_2 [-]	C_3 [-]
0.200	1500	0.635	0.291	900.0	1.070

Table 5. Exp.-numerically determined data and model predictions for DP600 ($l_0 = 0.2$ mm)

η [-]	0.032	0.100	0.162	0.246	0.348	0.649	0.743
$\bar{\theta}$ [-]	0.047	0.243	0.436	0.683	0.960	0.514	0.144
$\bar{\epsilon}_{pl}^f$ (experiment) [-]	0.886	0.839	0.805	0.823	0.842	0.671	0.449
$\bar{\epsilon}_{pl}^f$ (CrachFEM) [-]	0.843	0.820	0.810	0.809	0.824	0.594	0.527
$\bar{\epsilon}_{pl}^f$ (MMC) [-]	0.870	0.821	0.797	0.793	0.823	0.593	0.547

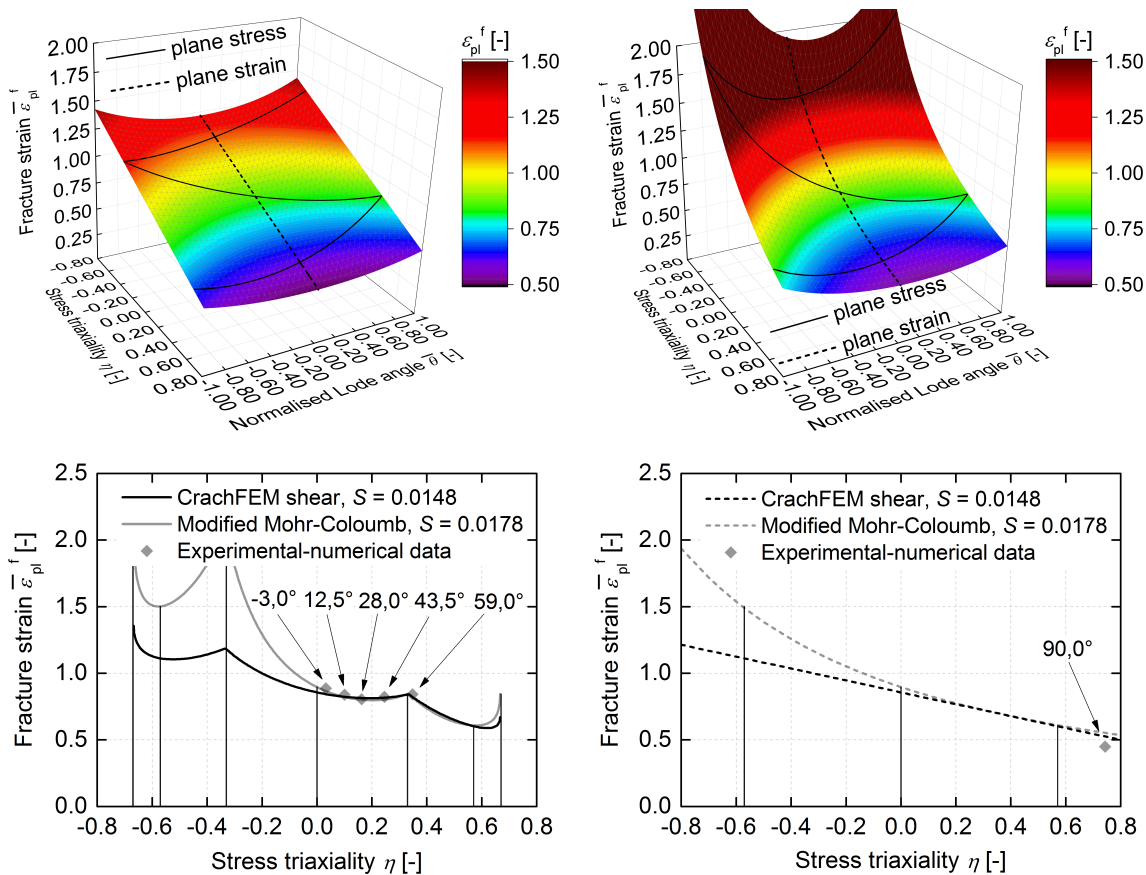


Figure 18. Fracture surfaces of DP600 according to the CrachFEM model (top left) and MMC model (top right) for the virtual gauge length of $l_0 = 0.2$ mm and fracture curves for plane stress (bottom left) and plane strain states (bottom right)

4. Conclusion and outlook

The work proved applicability of the new test on the new butterfly specimen to fracture characterisation of AHSS sheets. The advantages of the new specimen include an improved safety of fracture initiation at a desired stress state and decreased sensitivity of the plastic strain to the relative tool displacement. Furthermore, the new specimen exhibits less local material thinning during the test. The disadvantages of the new specimen remain in high production costs and fracture initiation at the machined surface at some load cases. The test allows material testing at two shear-tensile, two tensile-shear and one uniaxial tension plane stress states as well as two three-dimensional tensile stress states. For the five shear-tensile/tensile-shear plane stress states, determination of the fracture strain with digital image correlation is possible. For the other two stress states, other methods like FEA need to be used. In the future, material testing at five out of seven stress states seems to be more appropriate. The dependence of the fracture strain on the normalised Lode angle for DP600 was found to be less pronounced as it is often assumed. The dependence of the fracture strain on the space resolution of the FEA was found to be more pronounced for three-dimensional tensile stress states and negligible for compression-dominated stress states. Both the CrachFEM fracture model and MMC fracture model perform equally well in the studied range of stress states. The difference between the two models becomes notable for negative stress triaxialities only. The test procedure and results analysis are believed to contribute to current discussions on requirements to AHSS fracture characterisation.

Acknowledgments

Most of presented results were obtained in the frame of the projects P 972, P 1007 and P 1145 of the Research Association for Steel Application (FOSTA), Dusseldorf, Germany. The financial support of the FOSTA and technical support of the industrial project committees are gratefully acknowledged. From the industrial project committees, the authors especially thank Ford Forschungszentrum Aachen GmbH (A. Bach) for the provided material and Volkswagen AG (Dr. C. Sunderkötter) for funding of the tool manufacturing. Valuable support of Dr. B. Hackl (voestalpine Stahl GmbH) with the approximation of the fracture data is much appreciated.

References

- [1] Heuss R, Müller N, van Sintern W and Starke A 2012 *Lightweight, heavy impact* (McKinsey & Company)
- [2] Banabic D 2010 *Sheet Metal Forming Processes. Const. Modelling and Num. Simulation* (Berlin: Springer)
- [3] Roll K 2008 Simulation of sheet metal forming - necessary developments in the future *Proc. NUMIFORM (Interlaken)* (Zurich: IVP, ETH) pp 3-11
- [4] Keßler L and Gerlach J 2008 Industrial aspects of material modelling for steel grades in the past, present and future *Proc. NUMIFORM (Interlaken)* (Zurich: IVP, ETH) pp 13-17
- [5] Bao Y and Wierzbicki T 2004 A comparative study on various ductile crack formation criteria *J. Eng. Mater. Technol.* **126** pp 314-24
- [6] Hooputra H, Gese H, Dell H and Werner H 2004 A comprehensive failure model for crashworthiness simulation of aluminium extrusions *Int. J. Crash.* **9** pp 449-63
- [7] Wierzbicki T, Bao Y, Lee Y-W and Bai Y 2005 Calibraton and evaluation of seven fracture models *Int. J. Mech. Sci.* **47** pp 719-43
- [8] Till E and Hackl B 2013 Calibration of plasticity and failure models for AHSS sheets *Proc. IDDRG (Zurich)* (Zurich: Institute of Virtual Manufacturing, ETH) pp 119-24
- [9] Bai Y and Wierzbicki T 2013 The concept of damage accumulation for prediction necking and fracture of sheets *Proc. IDDRG (Zurich)* (Zurich: Institute of Virtual Manufacturing, ETH) pp 9-13
- [10] Walters CL 2009 Development of a punching technique for ductile fracture testing over a wide range of stress states and strain rates *PhD Thesis* (Cambridge: MIT)
- [11] Chottin J, Hug E and Rachnik M 2011 Damage accumulation in DP1000 sheets submitted to various stress states *Steel Res. Int. Proc ICTP* pp 895-900
- [12] Behrens B-A, Bouguecha A, Vucetic M and Peshekhodov I 2012 Characterisation of the quasi-static flow and fracture behaviour of DP steel sheets in a wide range of stress states *Arch Civ Mech Eng* **12** pp 397-406
- [13] Behrens B-A, Vucetic M and Peshekhodov I 2014 Effiziente Charakterisierung und Modellierung des Fließ- und Versagensverhaltens von DP-Stählen *Tagungsband des UKH* (Hanover: IFUM, LUH) pp 77-97
- [14] Keßler L, Richter H and Rösen H 2014 Die Anwendung von erweiterten Bewertungskriterien für die Simulation von Stahlwerkstoffen *Tagungsband des UKH* (Hanover: IFUM, LUH) pp 99 -109
- [15] Mohr D, Henn S 2007 Calibration of stress-triaxiality dependent crack formation criteria: A new hybrid experimental-numerical method *Exp Mech* **47** pp 805-820
- [16] Bai Y 2008 Effect of loading history on necking and fracture *PhD thesis* (Cambridge: MIT)
- [17] Peshekhodov I, Dykiert M, Vucetic M, Behrens B-A 2016 Evaluation of common tests for fracture characterisation of advanced high-strength sheet steels with the help of the FEA *IOP Conference Series: Materials Science and Engineering Proc. IDDRG (Linz)* (Bristol: IOP Publishing)
- [18] Behrens B-A, Vucetic M and Peshekhodov I 2014 Calibration of fracture initiation models for advanced high-strength sheet steels in a wide range of stress states using a uniaxial tensile testing machine *Proc. IDDRG (Paris)* (Senlis Cedex: CETIM) pp 252-57
- [19] Vucetic M, Bouguecha A, Peshekhodov I, Götze T, Huinink T, Friebe H, Möller T and Behrens B-A 2011 Num. validation of analytical biaxial true stress - true strain curves from the bulge test *Proc. NUMIFORM (Seoul)* (Melville: AIP) pp 107-14
- [20] Basaran M 2011 Stress state dependent damage modelling with a focus on the Lode angle influence *Dissertation* (Aachen: RWTH)
- [21] Bai Y, Wierzbicki T 2010 Application of extended MC criterion to ductile fracture *Int J Frac* **161** pp 1-20
- [22] Li Y, Luo M, Gerlach J, Wierzbicki T 2010 Prediction of shear-induced fracture in sheet metal forming *J Mat Proc Tech* **210** pp 1858-69
- [23] Mohr D, Marcadet SJ 2015 Micromechanically-motivated phenomenological Hosford-Coulomb model for predicting ductile fracture initiation at low stress triaxialities *Int J Sol Struc* **67-68** pp 40-55